

High Resolution *BOES* Spectroscopy of Raman-scattered He II λ 6545 in Young Planetary Nebulae

JIN LIM,¹ SEOK-JUN CHANG,² JAEJIN SHIN,¹ HEE-WON LEE,¹ JIYU KIM,¹ HAK-SUB KIM,^{1,3} BO-EUN CHOI,⁴ AND HO-GYU LEE⁵

¹*Department of Physics and Astronomy, Sejong University, Seoul, Korea*

²*Max-Planck-Institut für Astrophysik, Karl-Schwarzschild-Straße 1, 85748 Garching b. München, Germany*

³*Korea AeroSpace Administration, Sacheon, Korea*

⁴*Department of Astronomy, University of Washington, Seattle, WA 98195, USA*

⁵*Korea Astronomy and Space Science Institute, Daejeon, Korea*

ABSTRACT

Young planetary nebulae (PNe) are characterized by their hot central stars and the presence of abundant neutral and molecular components, which result from significant mass loss during the asymptotic giant branch (AGB) phase of stellar evolution. Far-UV He II λ 1025 line photons produced near the central star can undergo Raman scattering by hydrogen atoms, creating a broad emission feature centered at ~ 6545 Å. We conducted high-resolution spectroscopy of 12 young PNe from April 2019 to March 2020 using the Bohyunsan Observatory Echelle Spectrograph (*BOES*). Building on the study by Choi and Lee, who identified Raman-scattered He II at 6545 Å in NGC 6881 and NGC 6886, we report new detections of this feature in NGC 6741 and NGC 6884. Profile fitting reveals that the velocity of the H I component relative to the He II emission region ranges from 26 – 33 km s⁻¹ in these PNe. Using photoionization modeling, we estimate the line flux of He II λ 1025 and derive Raman conversion efficiencies of 0.39, 0.21, 0.24, and 0.07 for NGC 6881, NGC 6741, NGC 6886, and NGC 6884, respectively. These results, combined with radiative transfer modeling, suggest the presence of H I components with masses around $10^{-2} M_{\odot}$, moving outward from the central He II emission region at speeds characteristic of the slow stellar wind from a mass-losing giant star.

Keywords: Interdisciplinary astronomy(804)

1. INTRODUCTION

A star with mass $\leq 8 M_{\odot}$ loses a significant amount of its mass leaving behind a hot central core to become a planetary nebula (PN). A PN is characterized by an emission nebula that is photoionized by the hot central star. Young PNe are particularly important in the study of the mass loss process that characterizes the stellar evolution in the AGB stage. The slow stellar wind in the AGB stage mainly consists of molecules and dust grains with a significant contribution of neutral atomic species.

The strong far-UV radiation from the hot central star is believed to dissociate a significant amount of molecules into neutral species (e.g., Schneider et al. 1987). Natta & Hollenbach (1998) conducted extensive theoretical investigations into the evolution of neutral and molecular components in PNe. According to their modeling, the slowly expanding shell, primarily composed of dust and molecules, is further driven by the hot tenuous wind to reach a final speed of ~ 25 km s⁻¹.

As photodissociation progresses, the H I mass gradually increases, eventually reaching a maximum value of a few times $10^{-2} M_{\odot}$ in the case of a central star with mass $M_{*} = 0.6 M_{\odot}$. However, 21 cm radio observations of H I are severely hindered due to significant confusion from interstellar emission unless the object exhibits a substantial peculiar velocity relative to Galactic rotation (e.g., Schneider et al. 1987; Taylor et al. 1989, 1990). This limitation makes it challenging to trace neutral hydrogen components in a direct and reliable way (e.g., Höfner & Olofsson 2018).

Young PNe are also characterized by their compact size and the presence of high-excitation lines, including He II, which are produced by the central hot star. Considering the ionization potential of He II exceeds 50 eV, the He II emission nebula is photoionized by an extremely hot source. As a PN evolves, the nebula expands, and the temperature of the hot source decreases, making the duration of He II emission relatively short compared to the entire lifespan of the PN stage. Strong

He II emission and a compact size create favorable conditions for the Raman scattering of He II with atomic hydrogen to occur.

The first detection of Raman-scattered He II features in PNe was made by Péquignot et al. (1997) in the young PN NGC 7027. Subsequently, Raman-scattered He II features were identified in three young PNe: NGC 6302, IC 5117, and NGC 6790 (Groves et al. 2002; Lee et al. 2006; Kang et al. 2009). The detection of these spectral features indicates the presence of thick H I components with $N_{\text{HI}} \sim 10^{21-22} \text{ cm}^{-2}$. Raman-scattered He II features at 4850 Å in IC 5117 and NGC 6790 suggest that the H I components are moving away from the He II emission region with expansion speeds of $v_{\text{exp}} = 30$ and 20 km s^{-1} , respectively. From theoretical modeling of Raman-scattered He II formation using a Monte Carlo technique, the Raman conversion efficiency of He II $\lambda 6545$, amounting to $\sim 10\%$, is consistent with an H I mass of $\sim 10^{-2} M_{\odot}$ (e.g., Choi et al. 2020).

Recently, Choi & Lee (2020) reported the discovery of Raman-scattered He II at 6545 Å in NGC 6881 and NGC 6886. In this article, we present high-resolution spectroscopy of 12 young PNe and report our discovery of Raman-scattered He II at 6545 Å in two additional objects, NGC 6741 and NGC 6884, along with NGC 6881 and NGC 6886. In Section 2, we describe the basic atomic physics underlying the formation of Raman-scattered He II $\lambda 6545$ and its spectroscopic identification. In Sections 3 and 4, we present our spectra and perform line fit analysis to derive the relative velocity between the He II emission region and the H I region. In Section 5, we conduct photoionization computations and radiative transfer modeling to deduce the Raman conversion efficiency and estimate the H I mass. In the following section, we discuss the importance of Raman spectroscopy as a unique probe of PN evolution. Finally, in the last section, we summarize our results and outline directions for future work.

2. FORMATION OF RAMAN-SCATTERED HE II

Raman scattering involving atomic hydrogen offers a novel window for studying the distribution and kinematics of H I in young PNe. Raman scattering of a far-UV photon blueward of Ly α occurs when the photon interacts with a hydrogen atom in the ground state. This interaction causes the atom to de-excite to the 2s state while emitting a photon whose energy is reduced by the Ly α transition energy. As a single-electron species, He II has an energy level structure resembling that of atomic hydrogen. Nevertheless, the spacing between its energy levels is approximately four times wider. He II spectral lines from $2n \rightarrow 2$ transitions have shorter wavelengths

than the corresponding H I Lyman series ($n \rightarrow 1$). This difference arises because the reduced mass of He II is larger than that of H I by approximately the electron-to-proton mass ratio.

Quantitatively, the energy difference for H I and He II can be expressed as

$$\Delta E_n \simeq \frac{3}{4} \left(\frac{m_e}{m_p} \right) E_{\text{Ryd}} (1 - n^{-2}), \quad (1)$$

where E_{Ryd} denotes the Rydberg energy for hydrogen, and m_e and m_p represent the masses of the electron and proton, respectively. Thus, Raman scattering of He II produces an optical emission feature blueward of the nearby hydrogen Balmer line, with the wavelength difference given by

$$\Delta \lambda \simeq -5.9 \left[\frac{n^2(n^2 - 1)}{(n^2 - 4)^2} \right] \text{ \AA}. \quad (2)$$

Lee et al. (2001). Specifically, for Raman scattering of He II $\lambda 1025$, originating from the $6 \rightarrow 2$ transition, we find $\Delta \lambda = -18 \text{ \AA}$ with $n = 3$, leading to the formation of an optical line feature at 6545 Å. Figure 1 presents an energy level diagram illustrating the formation of Raman-scattered He II at 6545 Å. Interestingly, a spectral line, He II $\lambda 6527$, corresponding to the $n = 14 \rightarrow 5$ transition, is observed with a strength comparable to that of Raman-scattered He II at 6545 Å in young PNe (e.g., Lee & Hyung 2000; Choi & Lee 2020).

A very important spectroscopic feature of Raman scattering is that the Raman line profile width can differ significantly from that of the incident radiation. This difference arises from the transformation of wavelength spaces, as incident radiation in the far-UV regime is shifted to the optical region as Raman-scattered radiation. The energy conservation principle in the Raman scattering process establishes the relation:

$$\nu_{\text{inc}} = \nu_{\text{Ram}} + \nu_{\text{Ly}\alpha}, \quad (3)$$

where ν_{inc} , ν_{Ram} , and $\nu_{\text{Ly}\alpha}$ are the frequencies of the incident, Raman-scattered, and Ly α photons, respectively. Since $\nu_{\text{Ly}\alpha}$ is fixed, the variations in ν_{inc} and ν_{Ram} are equal. Consequently, the line widths of He II $\lambda 1025$ and Raman-scattered He II $\lambda 6545$ are related as:

$$\frac{\Delta \nu_{\text{inc}}}{\nu_{\text{inc}}} = \left(\frac{\nu_{\text{Ram}}}{\nu_{\text{inc}}} \right) \frac{\Delta \nu_{\text{Ram}}}{\nu_{\text{Ram}}} = \frac{1025}{6545} \frac{\Delta \nu_{\text{Ram}}}{\nu_{\text{Ram}}}. \quad (4)$$

This relationship indicates that the line width of Raman-scattered He II $\lambda 6545$ is broadened by a factor of 6.4 compared to that of the He II emission lines.

In addition to profile broadening, the expansion of wavelength space in Raman scattering should also

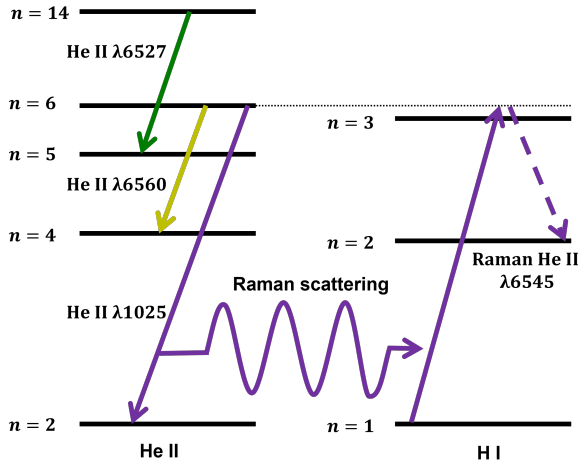


Figure 1. The energy levels of He II and H I relevant to formation of Raman-scattered He II at 6545Å. The green and yellow arrows represent optical He II emission lines near Raman-scattered He II.

be considered when determining the wavelength shift caused by the Doppler effect. When the H I region moves away from the He II emission region, the Raman He II feature shifts redward of the atomic line center. This shift follows the same expansion effect in wavelength space as described in Equation (4).

For example, if the relative velocity between the H I and He II regions is $+10 \text{ km s}^{-1}$, the Raman He II $\lambda 6545$ line shifts by approximately $+1.4 \text{ \AA}$ in wavelength space. Given the 3 \AA separation between Raman-scattered He II $\lambda 6545$ and $[\text{N II}]\lambda 6548$, a recession velocity of approximately 20 km s^{-1} for the H I region would result in complete blending of the two spectral features. Since the Raman-scattered He II $\lambda 6545$ feature is relatively weak, it is naturally expected to appear as broad wings around the $[\text{N II}]\lambda 6548$ line.

A careful spectroscopic analysis is required to detect the broad wings surrounding the $[\text{N II}]\lambda 6548$ emission line. Figure 2 presents a schematic illustration of the formation of various emission lines near $\text{H}\alpha$. The right panel displays *BOES* spectroscopic data of NGC 6881, showing broad spectral wings near $[\text{N II}]\lambda 6548$. Interestingly, $[\text{N II}]\lambda 6548$ is accompanied by $[\text{N II}]\lambda 6583$, which is nearly three times stronger (e.g., Osterbrock 1989). If $[\text{N II}]\lambda 6583$ does not display prominent broad wings, it strongly indicates that the wings around $[\text{N II}]\lambda 6548$ are not associated with nitrogen ions. This contributes to the identification of the broad wings as Raman-scattered He II $\lambda 6545$.

3. SPECTROSCOPIC OBSERVATION

With a view to searching for Raman-scattered He II features, we selected 12 PNe from the two catalogs pro-

vided by Tylenda et al. (1994) and Sahai et al. (2011). Tylenda et al. (1994) compiled the intensities of He II $\lambda 4686$ and $\text{H}\alpha$ lines for Galactic PNe, while Sahai et al. (2011) introduced a new morphological classification for 119 young PNe and determined their ages. We preferentially selected strong He II emitters with line intensity ratios of He II $\lambda 4686$ to $\text{H}\alpha$ greater than 0.05. Additionally, since young PNe are believed to contain a significant amount of neutral material including atomic hydrogen, we included some young PNe even if they have relatively low-intensity ratios.

We carried out deep high-resolution spectroscopy of the 12 PNe from April 2019 to March 2020 using the Bohyunsan Observatory Echelle Spectrograph (*BOES*; Kim et al. 2007) mounted on the 1.8 m telescope at the Bohyunsan Optical Astronomy Observatory. *BOES* is an optical fiber-fed echelle spectrograph covering a wavelength range of 3500–10500 Å. Raman-scattered He II features are expected to be broad and weak. To maximize the signal-to-noise ratio, we used the $300 \mu\text{m}$ fiber which yields a spectral resolution of $R (\equiv \lambda/\Delta\lambda) \sim 30000$, and used 2×2 binning. The total exposure time ranges from 600 to 3600 seconds depending on the target brightness. We also observed four spectrophotometric standard stars between our target observations.

The observation log, target list, and their basic information are given in Table 1. The data were reduced with the tasks in the *ccdred* and *echelle* packages in IRAF in a standard way including bias subtraction, extraction of spectral orders, and flat-field corrections. Wavelength and flux calibrations were performed using spectra of the Th–Ar lamp and spectrophotometric standards taken during the observations. We identify broad wings around $[\text{N II}]\lambda 6548$ in four targets, which we propose are the Raman-scattered He II $\lambda 6545$. The four objects are NGC 6881, NGC 6886, NGC 6741, and NGC 6884, and the first two of which were previously reported by Choi & Lee (2020).

We categorize our 12 target objects into three groups depending on the strength of He II emission lines and the detection of Raman-scattered He II $\lambda 6545$. If no He II emissions near $\text{H}\alpha$ are detected, the objects are classified as Group N (Non-detection). Group R consists of NGC 6881, NGC 6886, NGC 6741, and NGC 6884, where both He II emission at 6527 \AA and 6560 \AA and Raman-scattered He II at 6545 \AA are detected. The remaining objects that show a strong He II emission line at 6560 \AA , but no prominent Raman-scattered He II at 6545 \AA are classified as Group H.

In Figure 3, we show the *BOES* spectra of three PNe, each representing one of the three groups. In the left panel for NGC 6881, broad wings around $[\text{N II}]\lambda 6548$

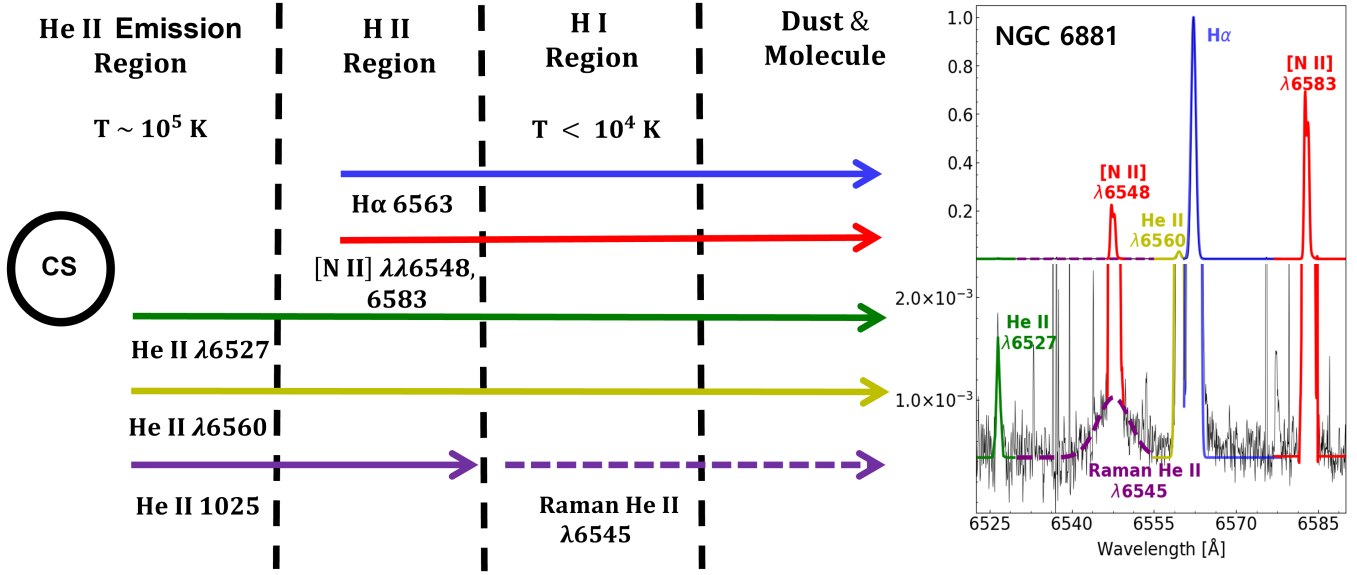


Figure 2. A schematic illustration of the formation of emission lines near $H\alpha$ (left) and the spectrum of NGC 6881 obtained with *BOES* (right). The central star (denoted by 'CS' inside a circle) is sufficiently hot to create a He II emission region with $T \sim 10^5$ K. Various emission lines are shown by colored arrows: He II $\lambda 6527$ (green), He II $\lambda 6560$ (yellow), [N II] $\lambda\lambda 6548$ and 6583 (red), $H\alpha$ (blue), He II $\lambda 1025$, and Raman He II $\lambda 6545$ (purple). On the right side, the spectrum is normalized to the peak of $H\alpha$. In the lower panel, the vertical scale is reduced to clearly reveal weak emission lines including He II $\lambda 6527$ and Raman-scattered He II $\lambda 6545$, the broad wing feature (purple dashed line) around [N II] $\lambda 6548$.

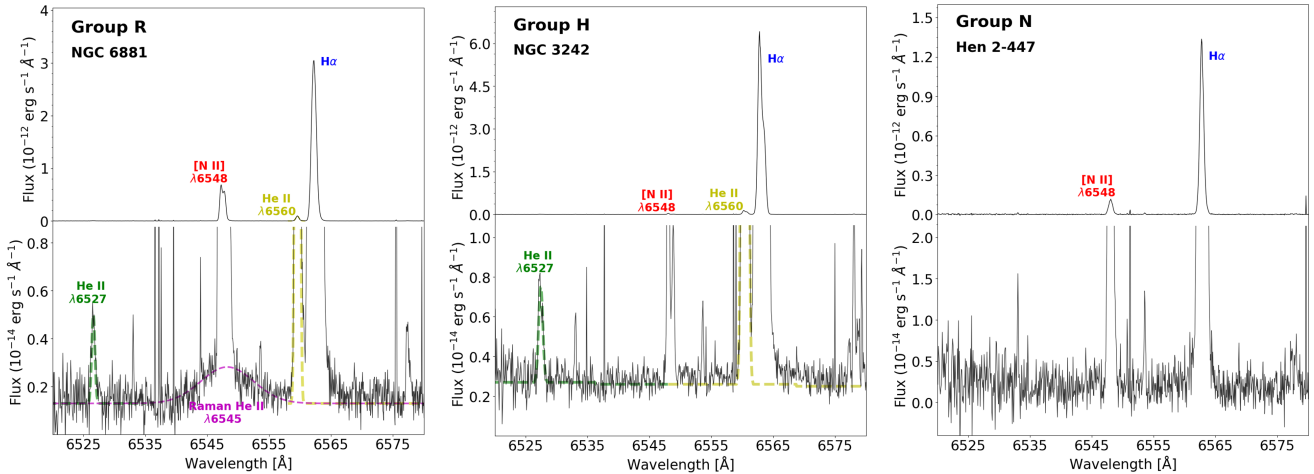


Figure 3. Representative spectra near $H\alpha$ of present three distinct groups: Group R, H, and N. Group R (left, NGC6881) exhibits both Raman-scattered He II $\lambda 6545$ and He II emission lines. Group H (center, NGC3242) shows a strong He II emission line at 6560 \AA but no Raman-scattered He II $\lambda 6545$. Group N (right, Hen2-447) shows no detection of Raman-scattered He II $\lambda 6545$ and He II emission lines in this *BOES* observation. The colors of the spectra correspond to the respective lines illustrated in Figure 2.

Table 1. Observational log for the 12 young PNe and their physical parameters.

Object	Date (yyyy-mm-dd)	Total Exposure Time (sec)	$\log T_{\text{eff}}$ (K)	$\log L/L_{\odot}$	Group [†]
H 4-1	2019-04-06	1800	5.11 ^a	2.28 ^a	N
Hu 2-1	2020-03-30	2400	4.51 ^b	4.06 ^b	
Hen 2-447	2019-06-05	600	5.03 ^c	2.77 ^c	
M 1-8	2020-03-30	3600	5.21 ^c	2.12 ^c	H
NGC 2346	2019-04-05	1800	4.76 ^c	3.84 ^c	
NGC 2392	2020-03-30	1200	4.90 ^d	4.41 ^d	
J 900	2019-04-06	1800	5.11 ^e	3.75 ^e	
NGC 3242	2020-03-30	3600	4.90 ^d	2.87 ^d	
NGC 6881	2020-03-30	3300	4.99 ^c	2.57 ^c	R
NGC 6886	2019-10-30	2400	5.18 ^d	2.83 ^d	
NGC 6741	2020-03-28	3600	5.23 ^f	2.75 ^f	
NGC 6884	2020-03-28	3600	4.90 ^c	3.27 ^c	

†: Three groups as shown in Figure 3. **a:** Otsuka et al. (2023), **b:** Miranda (1995), **c:** Stanghellini et al. (2002), **d:** Pottasch & Bernard-Salas (2010), **e:** Otsuka & Hyung (2020), **f:** Sabbadin et al. (2005).

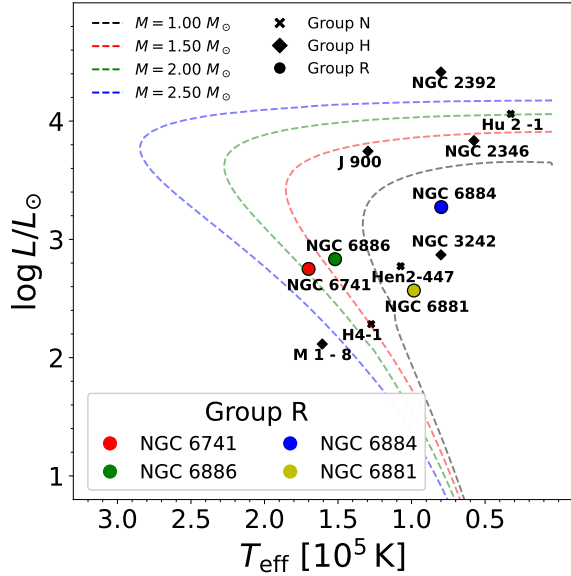


Figure 4. Evolutionary tracks between the AGB and the white dwarf phases for stars with the initial masses of 1.0, 1.5, 2.0, and 2.5 M_{\odot} obtained by Miller Bertolami (2016). The points are the temperature and luminosity of the young PNe considered in this paper, as shown in Table 1. Various marks are used to represent the three groups: Group R (circle), Group H (diamond), and Group N (cross). In particular, the four objects in Group R are shown with colored circles.

are apparent, which are identified with Raman-scattered He II $\lambda 6545$. It is notable that the strength of Raman-scattered He II is comparable to the near He II emission line at 6527 Å. In the middle panel for NGC 3242, no such wings are seen despite the clear detection of He II $\lambda 6527$ and He II $\lambda 6560$. The right panel shows the spectrum of Hen 2-447 with no detectable He II emission at 6560 Å.

The evolutionary track for PNe was investigated by many researchers (e.g., Miller Bertolami 2016). The temperature of the hot central star of a PN may reach 3×10^5 K. After the central star reaches the highest temperature, Raman scattering of He II will be suppressed due to weakening of He II $\lambda 1025$. In addition, the neutral material surrounding the central star will be dispersed into the interstellar space, which will lead to further suppression of He II Raman scattering.

Figure 4 shows the stellar evolution tracks between the AGB and white dwarf phases for stars with the initial masses of 1.0, 1.5, 2.0, and 2.5 M_{\odot} obtained by Miller Bertolami (2016). In this figure, the points, with different shapes based on classification, show the positions of the 12 PNe. Here, the temperature and luminosity are taken from the literature shown in Table 1. In particular, the filled circles correspond to the four PNe showing Raman-scattered He II feature at 6545 Å.

The 12 PNe observed with *BOES* are situated in a region characterized by very high temperatures, exceeding 3×10^4 K, and luminosities greater than $10^3 L_{\odot}$. Notably, four of these objects exhibiting Raman-scattered He II $\lambda 6545$ are closely interspersed with the other eight near the turning point. This raises the intriguing question of whether these four PNe in Group R can be distinctly identified using other independent observational factors. A preliminary inspection suggests a systematic trend of larger Balmer decrement in Group R objects. However, further studies targeting a larger sample of He II emitting PNe are necessary to draw definitive conclusions.

4. LINE PROFILE ANALYSIS

4.1. Gaussian fitting

To detect and analyze Raman-scattered He II, we perform a line fitting analysis for every visible emission line in the wavelength window of 6500–6600 Å (i.e., He II $\lambda 6527$, 6560 and H α). The analysis is carried out in three steps. First, we fit and subtract local continuum across 6500–6600 Å, determined from the emission-free windows of 6530–6540 Å and 6625–6635 Å. Secondly, we fit the emission lines in the continuum-subtracted spectrum. For He II $\lambda 6527$ and He II $\lambda 6560$, H α , which exhibit single-peak structures, we use a single Gaussian function given as

$$F(\lambda) = F_0 \exp[-(\lambda - \lambda_c)^2 / 2\Delta\lambda^2], \quad (5)$$

where F_0 , λ_c and $\Delta\lambda$ are the peak flux density, the observed line center and the width of the Gaussian function, respectively. In our line fitting analysis, we tie the kinematics between He II $\lambda 6527$ and He II $\lambda 6560$. The total line flux F_{tot} is given by

$$F_{\text{tot}} = \sqrt{2\pi} F_0 \Delta\lambda. \quad (6)$$

In contrast, for [N II] $\lambda 6548$, 6583, we use a double Gaussian function due to their prominent double-peak features. In the line fit analysis, the kinematics of these two lines is tied with the flux ratio fixed to be 1:3 (Osterbrock 1989). The best-fit parameters are determined by minimizing the sum of the chi-squared values. We correct the line widths by accounting for the instrumental resolution of *BOES* ($R \sim 30,000$).

Lastly, we mask [N II] $\lambda 6548$ and fit Raman-scattered He II $\lambda 6545$ separately. This is because of the severe blending between Raman-scattered He II $\lambda 6545$ and [N II] $\lambda 6548$. Note that we attempted to fit the two emission lines simultaneously but found that the fitting of Raman-scattered He II $\lambda 6545$ is heavily affected by the fitting result of [N II] $\lambda 6548$ due to its much weaker line

Table 2. Line fit parameters of the four objects in Group R

Line	Gaussian Fit Parameter	NGC6881	NGC6886	NGC6741	NGC6884
He II 6527	λ_c (Å)	6526.58	6526.83	6527.46	6526.11
He II 6560		6559.58	6559.86	6560.46	6559.10
Raman He II 6545		6548.23	6549.00	6548.70	6548.06
H α	F_{tot} (erg s ⁻¹ cm ⁻²)	2.9×10^{-12}	1.7×10^{-11}	2.5×10^{-11}	4.0×10^{-11}
He II 6527		2.4×10^{-15}	1.5×10^{-14}	2.9×10^{-14}	2.1×10^{-14}
He II 6560		6.0×10^{-14}	3.5×10^{-13}	4.3×10^{-13}	4.8×10^{-13}
Raman He II 6545		1.6×10^{-14}	6.3×10^{-14}	6.6×10^{-14}	2.7×10^{-14}
He II 6527	v_G (km s ⁻¹)	11	14	15	17
He II 6560		11	14	15	17
Raman He II 6545		196	173	194	123
	$v_G^{\text{Ram}*}$	31	27	30	19
	F_{6560}/F_{6527}	25	23	15	23
	$F_{6560}/F_{\text{H}\alpha}$	0.020	0.021	0.017	0.012
	ΔV_c (km s ⁻¹)	+29	+33	+26	+31

* The velocity width v_G^{Ram} of Raman-scattered He II $\lambda 6545$ in the parent velocity space of He II $\lambda 1025$ using Equation (8).

strength compared to [N II] $\lambda 6548$ (i.e., $\sim 1/500$). Therefore, we decide to fit Raman-scattered He II $\lambda 6545$ separately to avoid the contamination from [N II] $\lambda 6548$. In view of the fact that [N II] $\lambda 6548$ exhibits a double-peak structure in the four objects having Raman-scattered He II, the masking method is applied for both blue and red, within a 5σ threshold. After fitting, we determine the best-fit parameters of He II $\lambda 6545$ in the same manner as for the other lines.

In Figure 5, the observed data are shown by black solid lines. The green and yellow dashed lines show the fitting Gaussians for He II $\lambda 6527$ and He II $\lambda 6560$, respectively, while the purple dashed line is the Raman-scattered He II $\lambda 6545$. It is noted that Raman-scattered He II features are significantly broader than other He II emission lines.

In Table 2, we provide our fitting results for the four PNe in Group R. Here, instead of $\Delta\lambda$ we present the velocity width of the observed emission lines defined by

$$v_G = \left(\frac{\Delta\lambda}{\lambda_c} \right) c. \quad (7)$$

In the case of Raman-scattered He II $\lambda 6545$, the velocity width is computed in the parent velocity space so that

$$v_G^{\text{Ram}} = \frac{1}{6.4} \left(\frac{\Delta\lambda}{\lambda_c} \right) c, \quad (8)$$

where the factor 6.4 is the ratio of the frequencies of the incident and Raman-scattered photons.

4.2. Line Center Shift of Raman-scattered Line

In Figure 5, two vertical lines are drawn, where the red lines indicate the observed line center of He II $\lambda 6560$. From the atomic physics of He II Raman scattering, Raman-scattered He II $\lambda 6545$ is supposed to be formed at $\Delta v = -704$ km s⁻¹ from the line center of He II $\lambda 6560$. The atomic line centers, $\lambda_{6545}^{\text{atomic}}$ and $\lambda_{6560}^{\text{atomic}}$ adopted in this work are 6544.70 Å and 6560.10 Å, respectively (Hyung & Feibelman 2004; Lee et al. 2006; Chang et al. 2023). The blue vertical lines show the expected atomic center of Raman-scattered He II $\lambda 6545$ based on the position marked by the blue lines.

It is clearly noted that the observed Raman-scattered He II $\lambda 6545$ features are significantly redshifted with respect to the He II emission region, which we attribute to the expansion of the H I component with respect to the He II emission region. In order to determine the expansion speed, we may note that He II optical emission lines serve as velocity references for this purpose. The relative velocity ΔV_c between the H I and He II regions is determined by

$$\frac{\Delta V_c}{c} = \left(\frac{\lambda_{1025}^{\text{atom}}}{\lambda_{6545}^{\text{atom}}} \right) \frac{(\lambda_{6560}^{\text{atom}} - \lambda_{6545}^{\text{atom}}) - (\lambda_{6560}^{\text{obs}} - \lambda_{6545}^{\text{obs}})}{\lambda_{6545}^{\text{atom}}}, \quad (9)$$

where λ^{obs} and λ^{atom} are the wavelengths of the observed line center and the atomic line center, respectively. The velocity offset ΔV_c yields the same result when λ_{6560} is replaced with λ_{6527} .

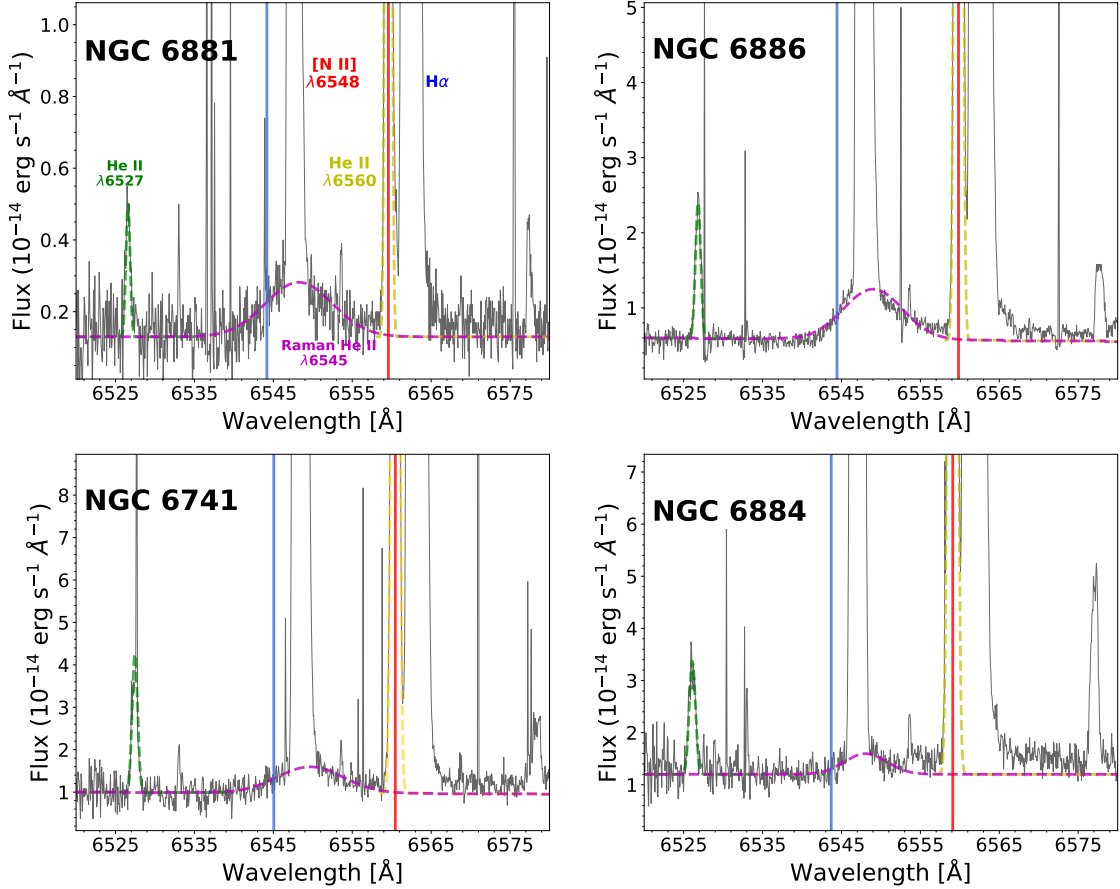


Figure 5. *BOES* spectra of NGC 6881, NGC 6886, NGC 6741, and NGC 6884 in Group R. These PNe have a relatively weak but broad Raman He II $\lambda 6545$ line blended with the strong [N II] $\lambda 6548$ line, along with clear He II $\lambda 6527$ and $\lambda 6560$ emission lines. The solid line represents the observed data, while the colored dashed lines denote the Gaussian fit. Colors green, yellow, and purple correspond to He II $\lambda 6527$, He II $\lambda 6560$, and Raman-scattered He II $\lambda 6545$, respectively. Two vertical colored lines are drawn, where the red lines indicate the observed center of He II $\lambda 6560$, and the blue lines mark the expected atomic line center of Raman-scattered He II $\lambda 6545$ based on the center line of He II $\lambda 6560$.

It is interesting that the relative velocities between H I and He II regions of the four objects are found in the considerably narrow range of $26 - 33 \text{ km s}^{-1}$, as shown in Table 2. This velocity range is consistent with the velocity scale expected of the slow stellar wind from stars on the AGB track (e.g., Höfner & Olofsson 2018). Taylor et al. (1990) carried out 21 cm observations to search the H I component in young PNe. In the case of NGC 6886, they found the expansion velocity of the H I component is $v_{\text{exp}} = 22.8 \pm 1.2 \text{ km s}^{-1}$.

5. PHOTOIONIZATION & RAMAN CONVERSION EFFICIENCY

To trace the H I mass in the vicinity of the He II emission region, it is essential to estimate the Raman conversion efficiency (RCE) and perform radiative transfer modeling. The Raman conversion efficiency is defined as

$$RCE_{6545} = \frac{\Phi_{6545}}{\Phi_{1025}}, \quad (10)$$

where Φ_{1025} and Φ_{6545} are the total number fluxes of He II $\lambda 1025$ and Raman-scattered He II $\lambda 6545$, respectively. However, the interstellar extinction is extremely heavy near the Lyman series of H I, making direct measurement of Φ_{1025} infeasible. One way to address this challenge is to use photoionization modeling, which allows us to deduce the flux ratio of He II $\lambda 1025$ to He II $\lambda 6560$. Using the flux ratio, Equation (10) can be rewritten as

$$RCE_{6545} = \left(\frac{\lambda_{0,6545}}{\lambda_{0,1025}} \right) \left(\frac{F_{6560}}{F_{1025}} \right) \left(\frac{F_{6545}}{F_{6560}} \right), \quad (11)$$

where $\lambda_{0,1025}$ and $\lambda_{0,6545}$ are the central wavelengths of He II $\lambda 1025$ and Raman-scattered He II $\lambda 6545$. This formulation relates the Raman conversion efficiency to observable fluxes and wavelengths, enabling indirect estimation even under conditions of strong interstellar extinction.

We use the Monte Carlo radiative transfer code *STaRS* Chang & Lee (2020) with a simple scattering geometry

to constrain the H I distribution that is consistent with the Raman conversion efficiency deduced from photoionization modeling. In Sections 5.1 and 5.2, we present the photoionization computations and radiative transfer modeling, respectively.

5.1. Photoionization Model of He II Emission

The publicly available photoionization modeling code CLOUDY (Ferland et al. 2017) is widely used to investigate the physical parameters of the observed spectra of PNe illuminated by their hot central stars (Barría et al. 2018; Otsuka & Hyung 2020; Galera-Rosillo et al. 2022; Gómez-Muñoz et al. 2024). Young PNe with detected Raman-scattered He II lines exhibit complex nebular morphologies, ranging from bipolar to prolate ellipsoidal shapes. This suggests that the He II emission regions may have intricate geometrical and kinematical structures (e.g., Santander-García et al. 2017; Balick et al. 2023).

In this work, we utilize CLOUDY with a simplified geometry to investigate the dependence of the He II flux ratio F_{6560}/F_{1025} on the physical conditions of the source and surrounding gas. A spherical nebula with uniform density, photoionized by black body radiation, is assumed. To further simplify the model, solar abundance is adopted. Three main parameters are considered: the hydrogen number density of the emission nebula, $n_H = 10^{3-7} \text{ cm}^{-3}$; the effective temperature of the central star, $T_{\text{eff}} = 50,000 - 300,000 \text{ K}$; and the stellar luminosity, $L_*/L_\odot = 10^{2-5}$.

In Figure 6, we present the computed He II flux ratio F_{1025}/F_{6560} as a function of T_{eff} . The left panel illustrates how the flux ratios vary with the hydrogen number density, n_H . In contrast, the right panel displays the flux ratios for different stellar luminosities, L_* . Across the range considered in our study, F_{1025}/F_{6560} increases from 4.6 to 5.5.

Consequently, we adopt the flux ratio $F_{1025}/F_{6560} = 5.15$, which represents the average value for T_{eff} at $n_H = 10^5 \text{ cm}^{-3}$ and $L_* = 10^4 L_\odot$, to compute the Raman Conversion Efficiency RCE_{6545} . With this flux ratio, Equation (11) simplifies to

$$RCE_{6545} = 1.24 \left(\frac{F_{6545}}{F_{6560}} \right). \quad (12)$$

Using the observed values listed in Table 2, we calculate the Raman conversion efficiencies for He II $\lambda 1025$ as 0.39, 0.24, 0.21, and 0.07 for NGC 6881, NGC 6886, NGC 6741, and NGC 6884, respectively.

5.2. Radiative Transfer Modeling

To investigate the distribution of H I consistent with the observed RCE_{6545} , we perform Monte Carlo simulations of the formation of Raman-scattered He II. For this purpose, we use the STARS code developed by Chang & Lee (2020), adopting the same scattering geometry as described in Choi et al. (2020).

Figure 7 describes a schematic illustration of the model geometry. In this scattering geometry, the H I region (blue) forms an open shell surrounding the central star, which is represented as a point-like He II emission region. The H I disk is defined by the half-opening angle θ_o and the H I column density N_{HI} (Chang et al. 2023). The dusty molecular region (green) is located outside the H I region. This structure is motivated by the observation of Raman-scattered He II lines in NGC 6302 (Chang et al. 2023), which is significantly obscured by dust (Kastner et al. 2022).

As long as the dusty region lies outside the H I region, He II $\lambda 1025$ photons are not affected by dust extinction before being Raman-scattered within the H I region. Additionally, both Raman-scattered He II $\lambda 6545$ photons and optical He II $\lambda 6560$ photons undergo nearly identical dust extinction due to their minimal wavelength difference. Consequently, the flux ratio of the observed He II $\lambda 6560$ to Raman-scattered He II $\lambda 6545$, as defined in Equation (11), determines the Raman conversion efficiency. This ratio remains unaffected by dust extinction because both lines are influenced equally.

In this simulation's scattering geometry, the H I medium expands away from the He II emission region with a velocity v_{exp} . Choi et al. (2020) demonstrated that the Raman conversion efficiency depends on the expansion velocity (see Figure 6). Additionally, Chang et al. (2023) presented model spectra of NGC 6302 based on Monte Carlo simulations for various expansion velocities of the Raman-scattered He II lines. Their findings suggest that a static H I region is inconsistent with the observed spectrum, strongly indicating the need to incorporate the expanding motion.

Our Monte Carlo simulation results are shown in Figure 8. The left panel presents the RCE_{6545} values for $\theta_o = 60^\circ$ at three different expansion velocities: $v_{\text{exp}} = 0$ (black), 20 (orange), and 30 km s^{-1} (red). The right panel displays the RCE_{6545} values computed over a range of θ_o and N_{HI} for $v_{\text{exp}} = 30 \text{ km s}^{-1}$, corresponding to the ΔV_c values for four objects in Group R (cf. Table 2). The contours (colored dashed lines) represent the RCE_{6545} values estimated for the four objects. For $\theta_o = 90^\circ$ and $N_{\text{HI}} > 10^{21} \text{ cm}^{-2}$, all He II $\lambda 1025$ photons undergo Raman scattering, resulting in $RCE_{6545} = 1$.

From the results shown in Figure 8, and assuming a scattering geometry with a column density of

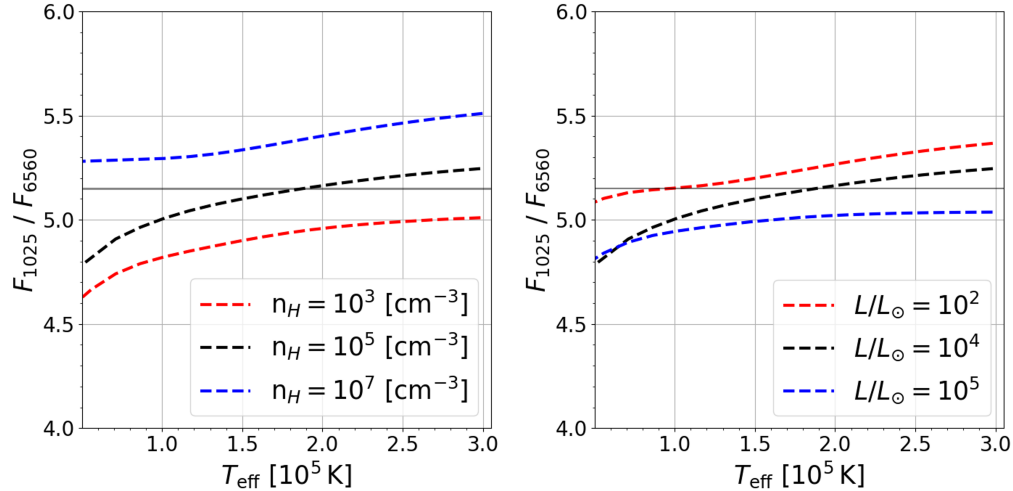


Figure 6. The flux ratios F_{1025}/F_{6560} for various values of T_{eff} obtained from our photoionization modeling using CLOUDY. The left panel displays the flux ratios for three values of $n_{\text{H}} = 10^3$ (red), 10^5 (black), and 10^7 cm^{-3} (blue) with fixed $L_* = 10^4 L_{\odot}$. In the right panel, the flux ratios are shown for three different values of the luminosity of the central star, $L_* = 10^2 L_{\odot}$ (red), $L_* = 10^4 L_{\odot}$ (black), and $L_* = 10^5 L_{\odot}$ (blue) with the number density fixed at $n_{\text{H}} = 10^5 \text{ cm}^{-3}$.

$N_{\text{HI}} = 10^{20.5} \text{ cm}^{-2}$, we estimate the H I masses to be $6 \times 10^{-2} M_{\odot}$, $5 \times 10^{-2} M_{\odot}$, $5 \times 10^{-2} M_{\odot}$, and $2 \times 10^{-2} M_{\odot}$ for NGC 6881, NGC 6886, NGC 6741, and NGC 6884, respectively. As N_{HI} and θ_{o} increase, multiple scattering effects become significant, leading to a more complex relationship between RCE_{6545} and the H I mass.

Choi & Lee (2020) set the column densities of NGC 6886 and NGC 6881 as $N_{\text{HI}} = 5 \times 10^{20} \text{ cm}^{-2}$ and $N_{\text{HI}} = 3 \times 10^{20} \text{ cm}^{-2}$, respectively. The H I masses of NGC 6881 and NGC 6886 are estimated to be $4 \times 10^{-2} M_{\odot}$ and $3 \times 10^{-2} M_{\odot}$, respectively. The differences in mass estimates are primarily attributed to the adopted values of N_{HI} . Additionally, they applied case B recombination theory to deduce He II $\lambda 1025$ and performed line fitting using simulated profiles instead of single Gaussian functions. Improving the H I mass estimates may require more intensive investigations with sophisticated scattering geometry.

The values of RCE_{6545} for NGC 6741 and NGC 6884 are lower than those for NGC 6881 and NGC 6886, where the detection of Raman-scattered He II was reported by Choi & Lee (2020). Particularly for NGC 6884, RCE_{6545} is less than 10 percent, making the Raman-scattered He II emission very weak. Additionally, the line width is considerably narrower compared to the other three objects. Choi et al. (2020) demonstrated that Raman-scattered He II lines can become significantly broadened due to multiple scattering in a very thick H I medium. The low RCE_{6545} and narrow line width observed for NGC 6884 are consistent with a smaller H I mass compared to the other three objects.

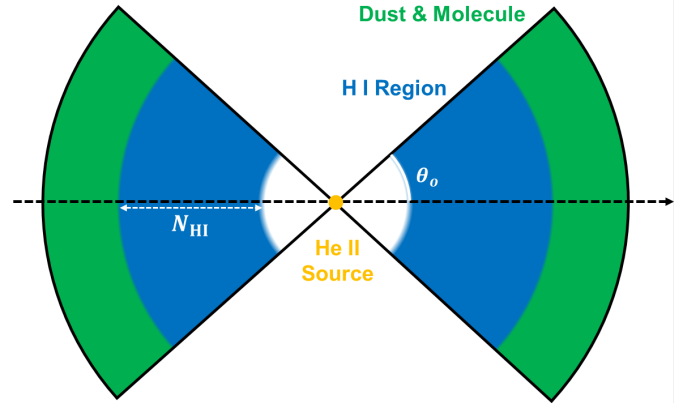


Figure 7. A schematic illustration of the model geometry composed of a point-like He II emission source (orange), an H I region (blue) characterized by H I column density N_{HI} and the half opening angle θ_{o} , and dusty molecular region (green).

6. DISCUSSION

6.1. Evolution of PNe and Raman Spectroscopy

The Raman scattering process of He II in PNe requires a thick H I region illuminated by a strong He II source. According to our photoionization model calculations using CLOUDY for a spherical nebula ionized by a central hot star, the strength of He II emission relative to H I is primarily determined by the temperature of the central ionizing source, with little dependence on the source's luminosity or the nebula's density. In the left panel of Figure 9, we present the flux ratio $F_{6560}/F_{\text{H}\alpha}$ for an

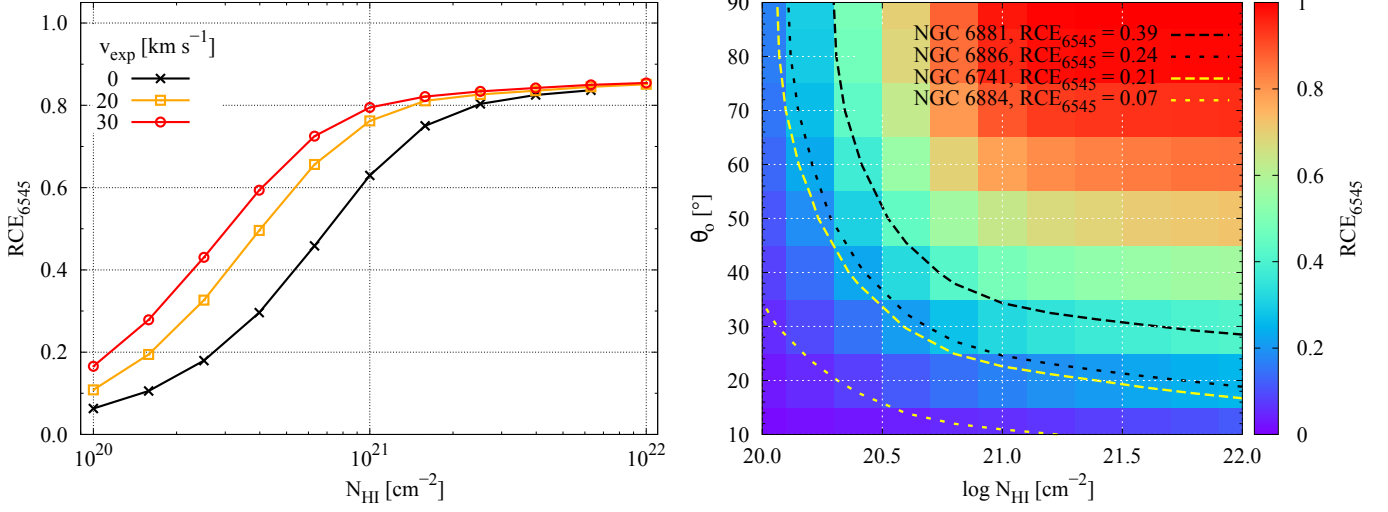


Figure 8. The Raman conversion efficiency, RCE_{6545} , is computed from Monte Carlo simulations using the *STaRS* code, assuming an H I disk geometry surrounding the central He II source. The left panel shows RCE values for $v_{\text{exp}} = 0$ (black), 20 (orange), and 30 km s^{-1} (red) as a function of N_{HI} with $\theta_0 = 60^\circ$. The right panel displays a map of RCE in the $N_{\text{HI}} - \theta_0$ plane for $v_{\text{exp}} = 30 \text{ km s}^{-1}$. The contours represent the observed RCE_{6545} values for NGC 6881 (black dashed), NGC 6886 (black dotted), NGC 6741 (yellow dashed), and NGC 6884 (yellow dotted).

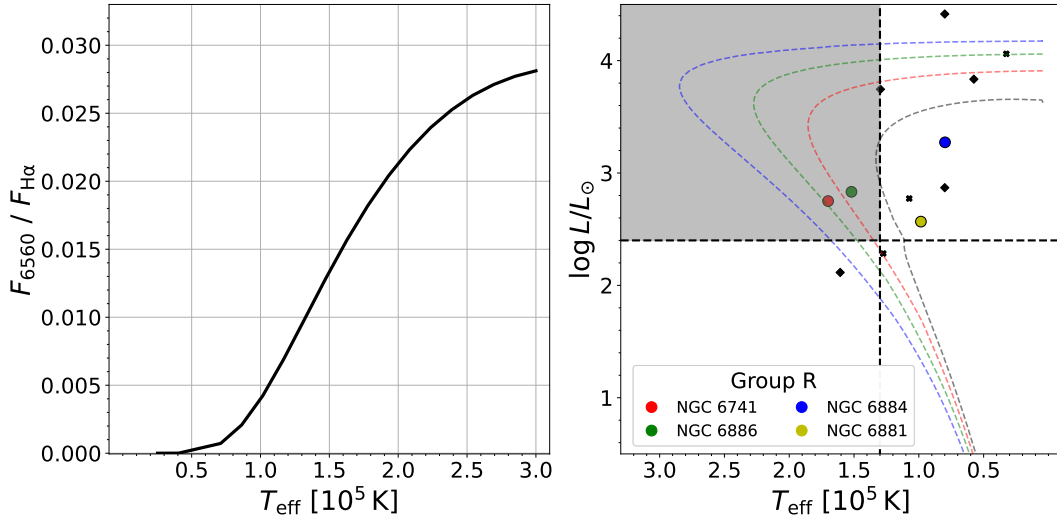


Figure 9. The flux ratio $F_{6560}/F_{\text{H}\alpha}$ computed using *CLOUDY* for an emission nebula characterized by our representative values $n_{\text{H}} = 10^5 \text{ cm}^{-3}$ and $L = 10^4 L_\odot$ for a range of T_{eff} (left), and the evolutionary tracks of planetary nebulae shown in Figure 4 (right). In the right panel, the vertical dotted line represents the temperature $T_{\text{eff}} = 1.3 \times 10^5 \text{ K}$ of the photoionization source that is required for $F_{6560}/F_{\text{H}\alpha} > 0.01$. The horizontal dotted line represents the lower bound for the luminosity of the PNe with Raman-scattered He II in our *BOES* data.

emission nebula characterized by representative values of $n_{\text{H}} = 10^5 \text{ cm}^{-3}$ and $L = 10^4 L_\odot$, while varying T_{eff} in the range $3.0 \times 10^4 \text{ K} < T_{\text{eff}} < 3.0 \times 10^5 \text{ K}$. The flux ratio is less than 0.001 for $T_{\text{eff}} = 50,000 \text{ K}$, while for $T_{\text{eff}} = 200,000 \text{ K}$, it increases to 0.02, which is typical of the He II emitting PNe in our sample (cf. Table 2).

The right panel of Figure 9 displays the evolutionary tracks of PNe, as illustrated in Figure 4. The shaded re-

gion, bounded by a vertical dotted line and a horizontal dotted line, approximately represents the evolutionary stage where Raman He II spectroscopy may play a significant role. The horizontal dotted line marks the lower luminosity bound of the PNe with Raman-scattered He II detected in our *BOES* data. As a PN evolves and crosses this horizontal line, Raman scattering of He II is severely suppressed due to the dilution of neutral material into

interstellar space, combined with the decreasing far-UV He II emission as the central star cools. The vertical dotted line indicates the temperature T_{eff} of the photoionizing source that results in a flux ratio $F_{6560}/F_{\text{H}\alpha} > 0.01$. This implies that strong He II-emitting PNe likely host central stars with $T_{\text{eff}} > 1.3 \times 10^5$ K. It is noted that two PNe—NGC 6881 (yellow) and NGC 6884 (blue)—are located outside the shaded region. However, given the strength of He II emission in these objects, it is highly likely that their temperatures are significantly underestimated. A detailed discussion of the uncertainties in measuring the temperature and luminosity of these objects is beyond the scope of this article.

Considering the significance of their evolutionary status near the turning point in the H-R diagram, a refined estimate of the population will offer crucial insights into the final stages of stellar evolution. A systematic spectroscopic survey of Raman-scattered He II lines could provide valuable clues about the photoionization and photodissociation processes occurring during the early stages of PN evolution.

6.2. Raman Wings around Balmer Lines

Another intriguing feature associated with Raman scattering by atomic hydrogen is the broad wings often observed in the Balmer emission lines of PNe. Notable examples are found in young PNe, including M2-9, IC 4997, IC 5117, and M3-27 (e.g., Balick 1989; Lee & Hyung 2000; Arrieta & Torres-Peimbert 2003; Ruiz-Escobedo et al. 2024). These wings can naturally form in a fast, hot stellar wind emanating from the central star. For instance, the far-UV spectrum of NGC 6543 exhibits prominent P Cygni profiles in the resonance O VI $\lambda\lambda 1032$ and 1038 lines, indicating the presence of a fast stellar wind with a velocity exceeding 10^3 km s $^{-1}$ (Perinotto et al. 1989).

Raman scattering by atomic hydrogen of far-UV radiation near the Lyman lines produces optical photons around the Balmer lines, leading to the formation of wings (Nussbaumer et al. 1989; Chang et al. 2018). Broad Balmer wings are commonly observed in symbiotic stars, which also exhibit Raman-scattered O VI and He II features. This suggests that the far-UV continuum near the Lyman series plays a significant role in the formation of Balmer wings in these objects.

7. SUMMARY AND FUTURE WORKS

We conducted deep, high-resolution spectroscopy of 12 young PNe using *BOES* and identified the Raman-scattered He II feature near 6545 Å in two additional young planetary nebulae, NGC 6741 and NGC 6884. These discoveries add to the previously reported detections in NGC 6881 and NGC 6886 by Choi & Lee (2020).

The strength of Raman-scattered He II depends on both the incident He II emission and the amount of H I surrounding the He II region. As the PN evolves, the amount of H I is expected to decrease as the entire nebula expands and the central star cools. Similarly, the relative strength of He II emission compared to H I is also expected to vary throughout the evolution of the PN.

The spectroscopic analysis of Raman-scattered He II $\lambda 6545$ is challenging due to severe blending with the strong [N II] $\lambda 6548$ line. In the cases of NGC 7027, NGC 6302, and IC 5117, Raman-scattered He II $\lambda 4850$ has been successfully detected (Péquignot et al. 1997; Groves et al. 2002; Chang et al. 2023). Unlike He II $\lambda 6545$, Raman-scattered He II $\lambda 4850$ is free from blending with other spectral features, allowing for more sophisticated theoretical modeling. However, our *BOES* observations are not deep enough to detect Raman-scattered He II $\lambda 4850$.

It is noteworthy that the detection of Raman-scattered He II has predominantly been limited to objects in the northern sky, with NGC 6302 being the only exception. This underscores the importance of conducting spectroscopic surveys aimed at identifying Raman-scattered He II features in the southern sky. By adopting a similar approach of targeting strong He II-emitting young planetary nebulae in the southern hemisphere, future spectroscopic surveys are expected to uncover a significantly larger number of objects exhibiting Raman-scattered He II.

Future observational strategies to study Raman-scattered features include spectropolarimetry and integral field unit (*IFU*) spectroscopy. He II recombination lines are naturally expected to be completely unpolarized. However, if the expanding neutral shell adopts a bipolar nebular morphology, introducing non-spherical symmetry in the scattering region, strong linear polarization is anticipated for Raman-scattered He II. Due to the faintness of Raman-scattered He II, conducting high-resolution spectropolarimetry is currently challenging. However, advancements in extremely large telescopes, such as the *Giant Magellan Telescope*, may enable such observations in the future (e.g., Ikeda et al. 2004).

The formation process of Raman-scattered He II suggests that He II emission is concentrated near the central hot star, whereas Raman-scattered He II is prominent in the neutral region moving away from the star. This implies that spectra extracted from the central region of a PN may differ significantly from those obtained in the peripheral regions. By combining positional and velocity information, it may be possible to describe the

various interactions between the ionized, neutral, and molecular components in these intriguing objects.

We are deeply grateful to the anonymous referee for his/her invaluable and constructive comments, which greatly enhanced the clarity and overall presentation of this paper. We thank the staff of the Bohyunsan Astronomical Observatory. This work was also supported by the National Research Foundation of Korea (NRF) grants funded by the Korea government (No. NRF-2023R1A2C1006984).

Facilities: BOAO(*BOES*)

Software: Cloudy (Ferland et al. 2013)

REFERENCES

- Arrieta, A., & Torres-Peimbert, S. 2003, *ApJS*, 147, 97, doi: [10.1086/374922](https://doi.org/10.1086/374922)
- Balick, B. 1989, *AJ*, 97, 476, doi: [10.1086/114996](https://doi.org/10.1086/114996)
- Balick, B., Borchert, L., Kastner, J. H., et al. 2023, *ApJ*, 957, 54, doi: [10.3847/1538-4357/acf5ea](https://doi.org/10.3847/1538-4357/acf5ea)
- Barría, D., Kimeswenger, S., Kausch, W., & Goldman, D. S. 2018, *A&A*, 620, A84, doi: [10.1051/0004-6361/201833981](https://doi.org/10.1051/0004-6361/201833981)
- Chang, S.-J., & Lee, H.-W. 2020, *Journal of Korean Astronomical Society*, 53, 169, doi: [10.5303/JKAS.2020.53.6.169](https://doi.org/10.5303/JKAS.2020.53.6.169)
- Chang, S.-J., Lee, H.-W., Kim, J., & Choi, Y.-H. 2023, *ApJ*, 949, 106, doi: [10.3847/1538-4357/acc868](https://doi.org/10.3847/1538-4357/acc868)
- Chang, S.-J., Lee, H.-W., Lee, H.-G., et al. 2018, *ApJ*, 866, 129, doi: [10.3847/1538-4357/aadf88](https://doi.org/10.3847/1538-4357/aadf88)
- Choi, B.-E., Chang, S.-J., Lee, H.-G., & Lee, H.-W. 2020, *ApJ*, 889, 2, doi: [10.3847/1538-4357/ab61f9](https://doi.org/10.3847/1538-4357/ab61f9)
- Choi, B.-E., & Lee, H.-W. 2020, *ApJL*, 903, L39, doi: [10.3847/2041-8213/abc559](https://doi.org/10.3847/2041-8213/abc559)
- Ferland, G. J., Porter, R. L., van Hoof, P. A. M., et al. 2013, *RMxAA*, 49, 137. <https://arxiv.org/abs/1302.4485>
- Ferland, G. J., Chatzikos, M., Guzmán, F., et al. 2017, *RMxAA*, 53, 385, doi: [10.48550/arXiv.1705.10877](https://doi.org/10.48550/arXiv.1705.10877)
- Galera-Rosillo, R., Mampaso, A., Corradi, R. L. M., et al. 2022, *A&A*, 657, A71, doi: [10.1051/0004-6361/202141890](https://doi.org/10.1051/0004-6361/202141890)
- Gómez-Muñoz, M. A., García-Hernández, D. A., Manchado, A., Barzaga, R., & Huertas-Roldán, T. 2024, *MNRAS*, 528, 2871, doi: [10.1093/mnras/stae218](https://doi.org/10.1093/mnras/stae218)
- Groves, B., Dopita, M. A., Williams, R. E., & Hua, C.-T. 2002, *PASA*, 19, 425, doi: [10.1071/AS02010](https://doi.org/10.1071/AS02010)
- Höfner, S., & Olofsson, H. 2018, *A&A Rv*, 26, 1, doi: [10.1007/s00159-017-0106-5](https://doi.org/10.1007/s00159-017-0106-5)
- Hyung, S., & Feibelman, W. A. 2004, *ApJ*, 614, 745, doi: [10.1086/423660](https://doi.org/10.1086/423660)
- Ikedo, Y., Akitaya, H., Matsuda, K., et al. 2004, *ApJ*, 604, 357, doi: [10.1086/381877](https://doi.org/10.1086/381877)
- Kang, E.-H., Lee, B.-C., & Lee, H.-W. 2009, *ApJ*, 695, 542, doi: [10.1088/0004-637X/695/1/542](https://doi.org/10.1088/0004-637X/695/1/542)
- Kastner, J. H., Moraga Baez, P., Balick, B., et al. 2022, *ApJ*, 927, 100, doi: [10.3847/1538-4357/ac51cd](https://doi.org/10.3847/1538-4357/ac51cd)
- Kim, K.-M., Han, I., Valyavin, G. G., et al. 2007, *PASP*, 119, 1052, doi: [10.1086/521959](https://doi.org/10.1086/521959)
- Lee, H.-W., & Hyung, S. 2000, *ApJL*, 530, L49, doi: [10.1086/312479](https://doi.org/10.1086/312479)
- Lee, H.-W., Jung, Y.-C., Song, I.-O., & Ahn, S.-H. 2006, *ApJ*, 636, 1045, doi: [10.1086/498143](https://doi.org/10.1086/498143)
- Lee, H.-W., Kang, Y.-W., & Byun, Y.-I. 2001, *ApJL*, 551, L121, doi: [10.1086/319830](https://doi.org/10.1086/319830)
- Miller Bertolami, M. M. 2016, *A&A*, 588, A25, doi: [10.1051/0004-6361/201526577](https://doi.org/10.1051/0004-6361/201526577)
- Miranda, L. F. 1995, *A&A*, 304, 531
- Natta, A., & Hollenbach, D. 1998, *A&A*, 337, 517
- Nussbaumer, H., Schmid, H. M., & Vogel, M. 1989, *A&A*, 211, L27
- Osterbrock, D. E. 1989, *Astrophysics of gaseous nebulae and active galactic nuclei* (California: University Science Books)
- Otsuka, M., & Hyung, S. 2020, *MNRAS*, 491, 2959, doi: [10.1093/mnras/stz3147](https://doi.org/10.1093/mnras/stz3147)
- Otsuka, M., Ueta, T., & Tajitsu, A. 2023, *PASJ*, 75, 1280, doi: [10.1093/pasj/psad069](https://doi.org/10.1093/pasj/psad069)
- Péquignot, D., Baluteau, J. P., Morisset, C., & Boisson, C. 1997, *A&A*, 323, 217
- Perinotto, M., Cerruti-Sola, M., & Lamers, H. J. G. L. M. 1989, *ApJ*, 337, 382, doi: [10.1086/167109](https://doi.org/10.1086/167109)
- Pottasch, S. R., & Bernard-Salas, J. 2010, *A&A*, 517, A95, doi: [10.1051/0004-6361/201014009](https://doi.org/10.1051/0004-6361/201014009)

- Ruiz-Escobedo, F., Peña, M., & Beltrán-Sánchez, A. V. 2024, MNRAS, 528, 4228, doi: [10.1093/mnras/stae247](https://doi.org/10.1093/mnras/stae247)
- Sabbadin, F., Benetti, S., Cappellaro, E., Ragazzoni, R., & Turatto, M. 2005, A&A, 436, 549, doi: [10.1051/0004-6361:20042447](https://doi.org/10.1051/0004-6361:20042447)
- Sahai, R., Morris, M. R., & Villar, G. G. 2011, AJ, 141, 134, doi: [10.1088/0004-6256/141/4/134](https://doi.org/10.1088/0004-6256/141/4/134)
- Santander-García, M., Bujarrabal, V., Alcolea, J., et al. 2017, A&A, 597, A27, doi: [10.1051/0004-6361/201629288](https://doi.org/10.1051/0004-6361/201629288)
- Schneider, S. E., Silverglate, P. R., Alschuler, D. R., & Giovanardi, C. 1987, ApJ, 314, 572, doi: [10.1086/165086](https://doi.org/10.1086/165086)
- Stanghellini, L., Villaver, E., Machado, A., & Guerrero, M. A. 2002, ApJ, 576, 285, doi: [10.1086/341340](https://doi.org/10.1086/341340)
- Taylor, A. R., Gussie, G. T., & Goss, W. M. 1989, ApJ, 340, 932, doi: [10.1086/167447](https://doi.org/10.1086/167447)
- Taylor, A. R., Gussie, G. T., & Pottasch, S. R. 1990, ApJ, 351, 515, doi: [10.1086/168489](https://doi.org/10.1086/168489)
- Tylenda, R., Stasińska, G., Acker, A., & Stenholm, B. 1994, A&AS, 106, 559

APPENDIX

A. HIGH RESOLUTION SPECTROSCOPY OF YOUNG PNE

In this appendix, we show our *BOES* spectra of young PNe belonging to Group N and Group H, in which no Raman-scattered He II was found.

In Figure A1, we show the *BOES* spectra of H 4-1, Hen 2-447, and Hu 2-1, in which we find no He II emission lines at 6560 Å. Furthermore, a close inspection of these objects shows that no He II λ 4686 is apparent in our *BOES* data. For example, Otsuka et al. (2023) presented spectroscopy of H 4-1 using the Kyoto University Seimei 3.8 m telescope, in which a clear presence of He II λ 4686 is noted. This strongly implies that our failure of He II detection in H 4-1 may be attributed to insufficient exposure in our observations.

In the top panels of Figure A2, we show our *BOES* spectra of M 1-8, NGC 2346 and NGC 2392. In these objects, we detect clearly He II λ 6560 emission line that appears as a blue shoulder of very strong H α . However, He II λ 6527 emission is not detected in these objects, implying insufficient data quality to search for Raman-scattered He II λ 6545. It should also be noted that the H α line of NGC 2392 is quite broad so that He II λ 6560 is embedded in the blue part of H α .

The lower two panels of Figure A2 show *BOES* spectra of J 900 and NGC 3242, where both He II λ 6560 and He II λ 6527 are clearly detected. In these objects, no wing features are noticeable around [N II] λ 6548, leading to nondetection of Raman-scattered He II λ 6545.

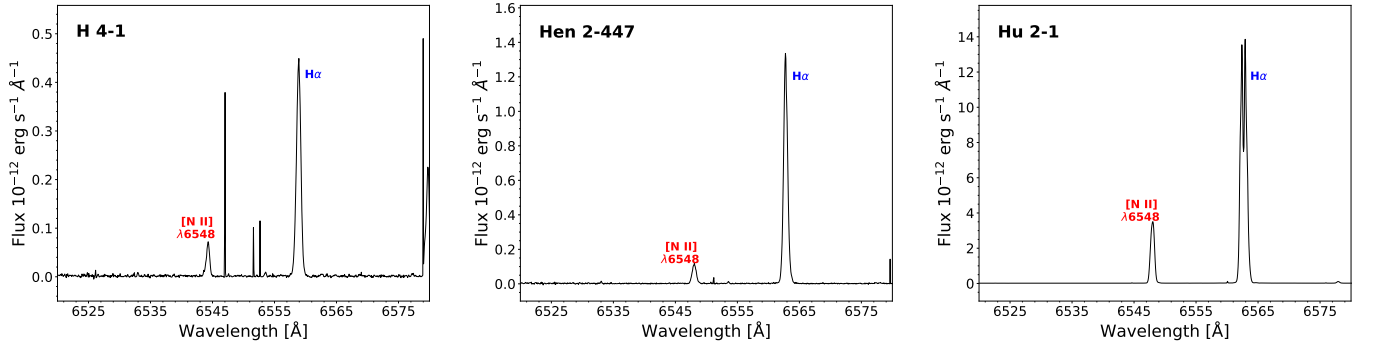


Figure A1. *BOES* spectra around H α of the young PNe H 4-1, Hen 2-447, and Hu 2-1 in Group N. Although these PNe are known to be He II emitters in the literature, neither He II λ 6560 nor He II λ 6527 is detected in our *BOES* data.

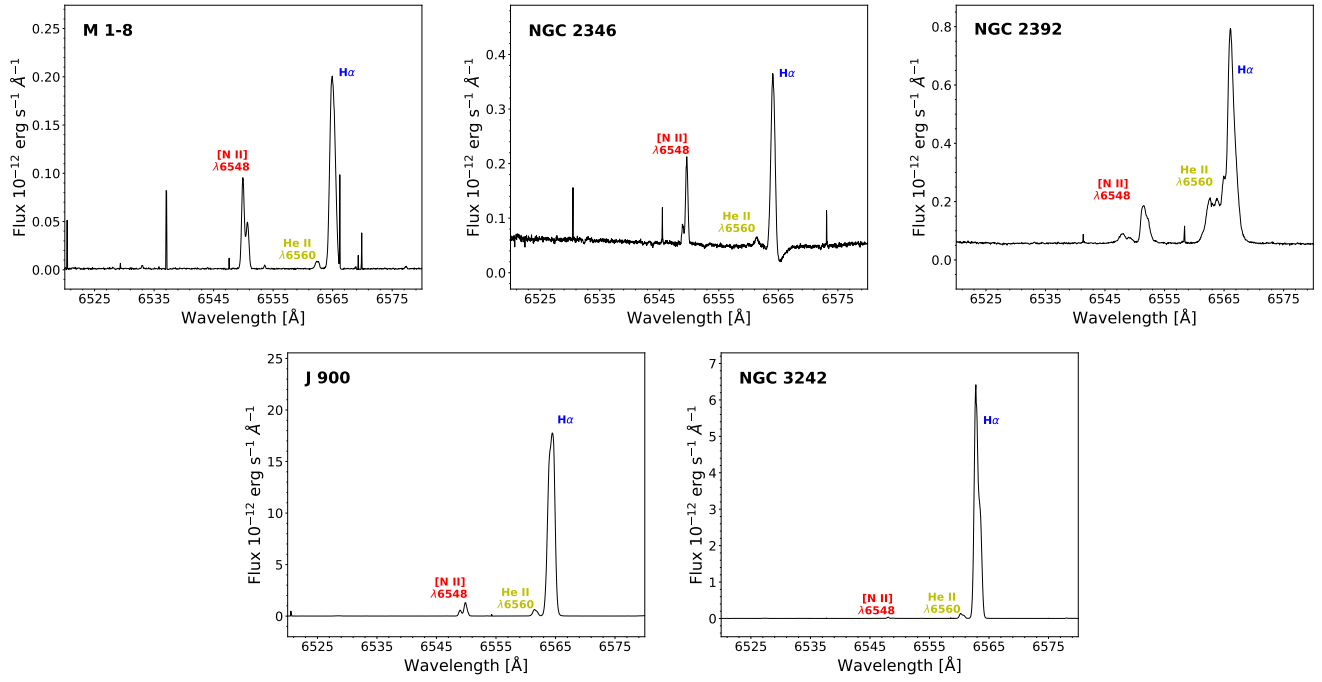


Figure A2. *BOES* spectra of M 1-8, NGC 2346, and NGC 2392 (top panels), J 900, and NGC 3242 (bottom panels) in Group H. In the top panels, He II $\lambda 6560$ line is visible but He II $\lambda 6527$ is not discernible for these PNe. In the bottom panels, He II $\lambda 6560$ and He II $\lambda 6527$ lines are detected for these two PNe.